Journal Pre-proof

Axial restraint effects on the cyclic performance and elongation behavior of T-shaped RC beams: Experimental and numerical investigations

Xi-Jun Chen, Xiao-Lei Han, Gui-Rui Lin, Jing Ji, Ji-Dong Cui

PII: S2352-7102(26)01682-7

DOI: https://doi.org/10.1016/j.jobe.2026.116860

Reference: JOBE 116860

To appear in: *Journal of Building Engineering*

Received Date: 17 May 2026

Revised Date: 28 June 2026

Accepted Date: 9 July 2026

Axial restraint effects on the cyclic performance and elongation behavior of T-shaped RC beams: Experimental and numerical investigations

Xi-Jun Chen [a,b], Xiao-Lei Han [a,b], Gui-Rui Lin [a,b], Jing Ji [a,b] *, Ji-Dong Cui [c]

[a] State Key Laboratory of Subtropical Building and Urban Science, South China University of Technology, Guangzhou, China

[b] School of Civil Eng. & Transportation, South China University of Technology, Guangzhou, China.

[c] China Energy Engineering Group Guangdong Electric Power Design Institute Co., Ltd, Guangzhou, China.

Abstract

To investigate the cyclic performance and axial elongation behavior of T-shaped RC beams under axial restraint, three full-scale specimens with a shear-span ratio of 4 were tested under quasi-static cyclic loading, including one unrestrained specimen and two restrained specimens with low and high axial restraint levels. The results showed that both axial elongation and residual elongation ratio decreased with increasing restraint stiffness, indicating stronger suppression of the unrecoverable residual component than the recoverable geometric component. Beam elongation under restraint generated restraint-induced axial compression, which increased with restraint stiffness and enhanced flexural capacity. The backbone curves exhibited post-yield hardening due to restraint-induced axial compression, together with asymmetric responses caused by slab action, with higher peak lateral loads and more gradual post-peak strength degradation under negative loading. The maximum restraint-induced axial compression reached 576 kN, and the maximum overstrength ratio reached 96%, suggesting that axial restraint may significantly influence beam-end force demands and force redistribution in RC frames. Axial restraint also enhanced lateral stiffness and energy dissipation capacity, with cumulative energy dissipation increasing by 21% and 42% for the low- and high-restraint specimens, respectively. ABAQUS finite-element models were established and validated against the tests, with maximum errors of less than 11% for peak lateral load and 17% for axial elongation. Numerical analyses further indicated that restrained T-shaped beams may be evaluated as compression-bending members for flexural capacity assessment, although this simplification cannot reproduce the full hysteretic response. Further validation is needed to extend these findings beyond the investigated specimens and restraint conditions.

Keywords: T-shaped RC beam; Beam elongation; Axial restraint; Cyclic loading; Finite-element simulation

---

* *Corresponding author. email: cvjingji@scut.edu.cn*

1. Introduction

Reinforced concrete (RC) frame structures are prone to severe damage under strong earthquakes. As the primary lateral force-resisting and energy-dissipating members in frame structures, RC beams are intended to undergo inelastic deformation and concentrate damage in beam-end plastic hinge regions. Under cyclic loading, RC beams develop axial elongation as plastic hinges form and rotate [1–3]. This elongation is primarily caused by flexural crack opening and the accumulation of tensile plastic strains in the longitudinal reinforcement [4]. Experimental studies have shown that, before concrete crushing occurs, the axial elongation of RC beams can reach up to 5% of the beam depth [4–8]. Based on these experimental observations, several numerical studies have been conducted to predict the axial elongation response of RC beams [8–11]. Wu et al. [9] pointed out that axial elongation consists of recoverable geometric and unrecoverable residual components, both of which are strongly correlated with the flexural rotation of the plastic hinge. Lee et al. [10] noted that axial deformation in the plastic hinge region is more pronounced under cyclic loading than under monotonic loading, and proposed a method for predicting the axial deformation of RC beams under different loading conditions.

However, when RC beams are incorporated into frame structures, their axial elongation is not free to develop but is restrained by adjacent columns, thereby inducing axial compression in the beams [12–17]. Tests by Yi et al. [14] showed that the flexural capacity of restrained beams increased by 20% compared with that of unrestrained beams. Similar overstrength behavior has also been observed in restrained beam-column subassemblies. Wang et al. [18] reported axial compression ratios as high as 0.25, accompanied by flexural overstrength ranging from 40% to 150%. Luo et al. [19] showed that this overstrength was strongly influenced by the longitudinal reinforcement ratio, with lower reinforcement ratios leading to more pronounced overstrength and an overstrength ratio of up to 155% when the reinforcement ratio was 0.44%. Significant overstrength induced by beam-elongation restraint has been consistently observed in both experimental and numerical investigations [20–26], with some studies reporting overstrength ratios exceeding 200% [26].

Such restraint-induced beam overstrength poses a significant challenge to the seismic design philosophy of strong-column-weak-beam mechanisms. Current seismic design provisions commonly require column flexural strength to exceed beam flexural strength by 20%–30% to ensure that inelastic deformation is concentrated in beams [27–31], which is much lower than the overstrength values reported above [20–26]. This may lead to strong-beam effects and increase the risk of damage concentration in columns or beam-column joints. In addition to increasing beam flexural capacity, restraint-induced axial compression can also amplify force demands on adjacent structural members. Previous studies reported increases of up to 49.7% in column shear demand and 241%–302% in exterior column-end moment demand [32], together with increases of 61%–120% in interior joint shear demand [18]. Therefore, beam elongation, restraint-induced axial compression, and the resulting flexural overstrength should be considered in capacity design to better evaluate the additional force demands imposed on adjacent columns and beam-column joints.

To maintain the intended capacity design hierarchy and ensure that RC beams function effectively as energy-dissipating members during earthquakes, it is crucial to accurately assess their seismic performance, particularly axial elongation, restraint-induced axial compression, and flexural capacity under axial restraint. Although these restraint-related responses of RC beams have been investigated in previous studies, most existing research has focused on rectangular beams. In practical RC frame systems, however, beams are rarely isolated rectangular members; they are typically cast with slabs, forming T-shaped or L-shaped cross-sections [33–34]. This interaction with the slab can significantly influence the failure modes, flexural capacity, ductility, and axial elongation behavior of the beams [35–37]. Santarsiero et al. [35] observed that slabs significantly improved the flexural strength of beams, with enhancements of up to 125% when the slab was subjected to compression. Ning [36] performed quasi-static tests on RC frames and reported that cast-in-situ slabs increased the lateral capacity by 15% and the ductility coefficient by 18% compared with the bare frame. Similarly, Zheng et al. [37] experimentally and numerically investigated RC frames and found that, compared with the control rectangular simply supported beams, beams cast with slabs exhibited up to a 300% increase in flexural capacity, whereas their ductility index was only 76% of that of the control beams. They further pointed out that slab action significantly affected beam axial elongation, which may in turn influence the associated restraint-induced axial compression. Despite these advances, limited attention has been paid to the elongation restraint behavior of RC beams with slab participation, and the assessment of restraint-induced overstrength in practical RC frames remains insufficiently clarified.

To address these gaps, three full-scale T-shaped beam specimens with different restraint stiffness levels were tested under quasi-static cyclic loading. The failure characteristics, hysteretic behavior, flexural capacity, axial elongation, and restraint-induced axial compression of the specimens were investigated. Based on the experimental results, an ABAQUS finite-element model was developed and validated against the experimental results. Using the validated model, the stress and damage distributions of the specimens were further analyzed. Additional simulations under constant axial compression were conducted to evaluate the influence of axial compression on flexural capacity and to examine the feasibility of treating restrained T-shaped beams as compression-bending members for flexural capacity assessment.

2. Experimental design

2.1 Specimen design

To investigate the mechanical behavior of RC beams under axial restraint during cyclic loading, three T-shaped beam specimens were designed with restraint stiffness as the variable. Previous studies have examined the restraint imposed by adjacent members on beam elongation in RC frame structures [11,18,26]. In this study, a steel-rod restraint system was used to provide an equivalent axial restraint stiffness representing the restraint imposed on beam elongation by the surrounding frame system. This equivalent stiffness was determined using thermal analogy-based analysis [32], in which the stiffness contributions from directly connected columns, columns in adjacent stories, and columns in adjacent bays were considered. Based on this analysis and reported stiffness ranges for restrained RC beams, two axial restraint stiffness values of 30 kN/mm and 99 kN/mm were selected to represent low and high axial restraint conditions, respectively, while the unrestrained specimen was used as the reference specimen. These stiffness values are also consistent with the restraint stiffness range reported in previous studies on restrained RC beams and frame systems [18,19,26,32].

All specimens exhibited a rectangular web section with a width b_w of 200 mm and a depth h_w of 500 mm, satisfying the minimum section dimensions required by the code [38] and representing a beam section commonly used in engineering practice. The slab thickness h_f was taken as 100 mm, and the slab was reinforced with two layers of D8 bars spaced at 200 mm, both of which are representative of commonly used RC floor slab detailing. The flange width was determined according to the effective flange-width provisions for T-shaped beams specified in the code [38]. Specifically, the effective flange width was taken as $6h_f$ on each side of the web, resulting in a total flange width bf of 1400 mm. The adopted shear-span ratio λ, relatively low longitudinal reinforcement ratios ρ_s, and relatively high transverse reinforcement ratio ρ_{sv} were selected to provide sufficient flexural deformation capacity and promote flexure-dominated failure, thereby allowing beam elongation to develop for investigating the effects of axial restraint.

Fig. 1 shows the dimensions and reinforcement details of the specimens. Table 1 presents the design parameters of the specimens, including the total length L_t, effective loading length L_0, shear-span ratio λ, single-sided longitudinal reinforcement ratio ρ_s, transverse reinforcement ratio ρ_{sv}, axial restraint stiffness K_r, and restraint coefficient κ [26]. The specimens were designated as TB0, TB1, and TB2, where “TB” denotes “T-shaped beam”, and the numbers 0, 1, and 2 represent the unrestrained, low-restraint, and high-restraint conditions, respectively.

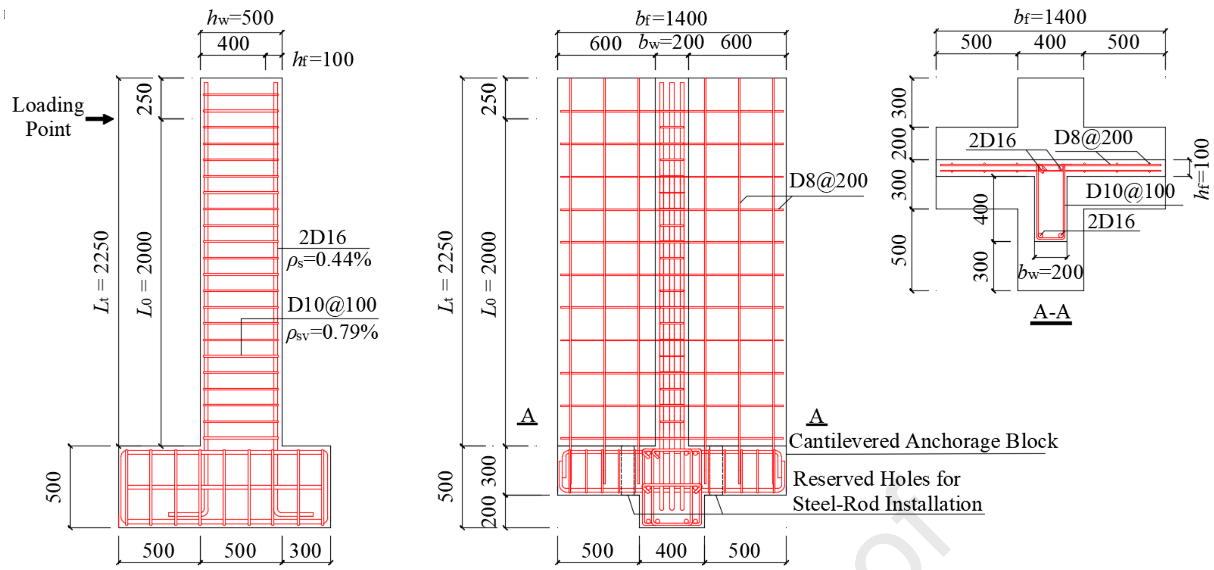

Fig. 1. Dimensions and reinforcement details of the specimens

Table 1

Design parameters of the specimens

Specimen	h_w (mm)	b_w (mm)	h_f (mm)	b_f (mm)	L_t (mm)	L_0 (mm)	λ	ρ_s (%)	ρ_{sv} (%)	K_r (kN/mm)	κ
TB0	500	200	100	1400	2250	2000	4.0	0.44	0.79	0	0.00
TB1	500	200	100	1400	2250	2000	4.0	0.44	0.79	30	0.01
TB2	500	200	100	1400	2250	2000	4.0	0.44	0.79	99	0.03

2.2 Material properties

As shown in Fig. 2, concrete specimens and reinforcement samples from the same batches were prepared during specimen fabrication and tested to determine their material properties.

Fig. 2. Specimen fabrication and material property tests

The concrete cube compression tests were conducted in accordance with the relevant code

[39]. The average cubic compressive strength measured from 150 mm concrete cubes was 32.94 MPa. Since the elastic modulus and tensile strength were not directly measured, they were estimated from the measured cubic compressive strength according to the relevant code [38]. The estimated elastic modulus and tensile strength were 30.74 GPa and 2.70 MPa, respectively. The properties of the steel reinforcement with different diameters were measured in accordance with the relevant code [40], and the results are listed in Table 2.

Table 2

Material properties of reinforcement

Diameter of reinforcement (mm)	Reinforcement Type	Yield strength (MPa)	Ultimate strength (MPa)
8	Slab reinforcement	404	620
10	Transverse reinforcement	420	613
16	Longitudinal reinforcement	451	620

2.3 Test setup and loading protocol

As shown in Fig. 3, fixed beams and jacks were installed during testing to prevent out-of-plane movement of the specimen during loading. The actuator was connected to the specimen at a loading point 250 mm below the specimen top. The main monitored quantities included load, displacement, axial elongation, and restraint-induced axial compression. Axial restraint was applied using two high-strength steel rods, with different rod diameters used to achieve different levels of axial restraint stiffness. The upper ends of the rods passed through a loading steel beam positioned at the top of the specimen, whereas the lower ends were anchored to the cantilevered anchorage blocks extending from the foundation beam. Spherical hinges were installed at both ends of the rods to allow axial-force transfer while minimizing unintended bending moments.

During testing, the axial compression induced by restrained elongation was measured using ring-type pressure transducers installed on each restraint rod above the loading steel beam, between the spherical hinge and the anchorage nut. Displacements were recorded using linear variable differential transformers (LVDTs). L1 measured the loading displacement, while L2 and L3 measured the left and right axial deformations of the specimen at the loading point, respectively. The axial elongation at the section centroid was then calculated by linear interpolation between the L2 and L3 readings.

It should be noted that the cantilevered anchorage blocks connected to the steel rods were locally strengthened and checked to behave as nearly rigid force-transfer regions. In addition, the reported axial elongation and restraint-induced axial compression were based on direct force and displacement measurements during loading and therefore represent the actual effective axial restraint condition of the specimens.

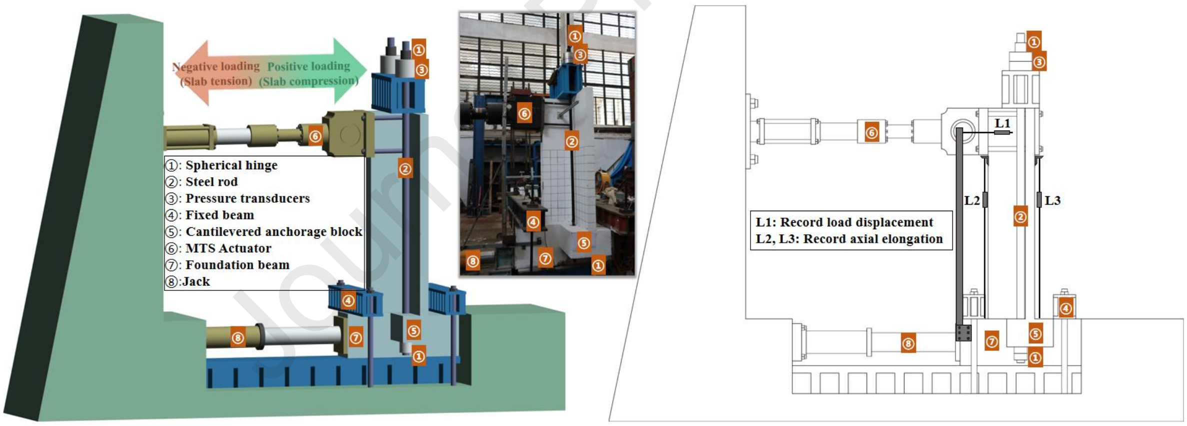

(a) Loading device (b) Layout of displacement meter

Fig. 3. Test setup and instrumentation

Cyclic loading was applied to the specimens under displacement control, with positive and negative loading corresponding to slab compression and slab tension, respectively. Before testing, the displacement corresponding to first yielding of the longitudinal reinforcement was preliminarily estimated, and the corresponding drift ratio was approximately 1/250. Therefore, the displacement corresponding to a drift ratio of 1/250 was adopted as the nominal yield displacement Δ_y for loading control. In the initial loading stage, one cycle was applied at each drift ratio of 1/2000, 1/1000, 1/500, and 3/1000. Thereafter, Δ_y was used as the displacement increment, and three cycles were imposed at each subsequent displacement level starting from 1/250. It should be noted that Δ_y was used only to define a unified displacement increment for the cyclic loading protocol. This unified loading protocol enabled direct comparison of specimen responses at the same drift levels. Loading was continued until the load decreased to 80% of the peak load, at which point the specimen was considered to have failed. The detailed loading protocol is shown in Fig. 4.

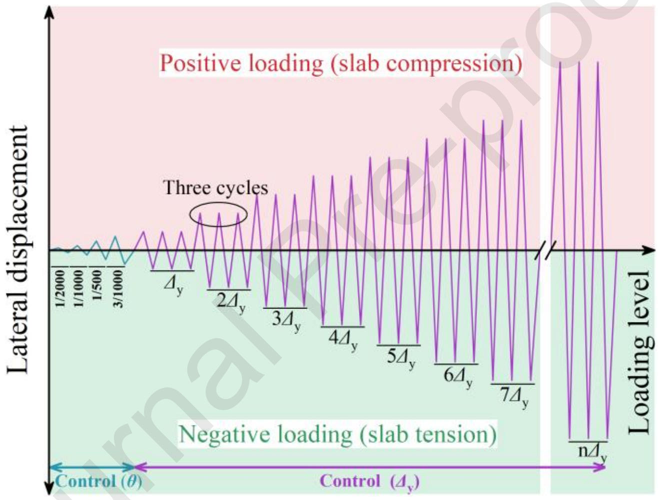

Fig. 4. Loading program

3. Experimental results and discussion

3.1 Failure phenomena

Fig. 5 shows the failure patterns of the three specimens. The specimens exhibited similar damage progression throughout the loading process. In the initial loading stage, horizontal cracks first appeared at the beam bottom. As loading proceeded, these cracks propagated and widened, and additional cracks formed above the initial ones.

(a) Crack appearance (b) Plate cracking (c) Concrete scaling

R_{DA}=10% 100mm×100mm+0.5×100mm×200mm (d) Specimen failure (TB0)
R_{DA}=15% 0.5×200mm×300mm (e) Specimen failure (TB1)
R_{DA}=20% 100mm×200mm+200mm×100mm (f) Specimen failure (TB2)

Fig. 5. Failure patterns of the specimens

At yielding, the cracks had extended through the beam section. With further loading, new cracks continued to form in both the beam and the slab, and several inclined cracks appeared under cyclic loading. Meanwhile, the cracks at the beam bottom became more pronounced. As loading approached the peak load, the cracks continued to propagate and widen. Under negative loading, concrete spalling initiated at the beam bottom and progressively intensified until failure. In contrast, under positive loading, the slab flange provided enhanced compressive resistance, and no obvious concrete spalling was observed near the flange region. The final damage was mainly concentrated at the beam bottom, where concrete spalling developed, whereas little further damage was observed in the other regions.

Although the three specimens showed similar overall failure progression, their local damage characteristics varied with restraint stiffness. For TB0, a horizontal crack approximately 250 mm long first appeared at a drift ratio of 1/1000, with a maximum crack width of 0.1 mm. Cracks penetrating the slab and beam sections were observed at drift ratios of 1/500 and 1/250, respectively, with inclined cracks also developing at a drift ratio of 1/250. At this stage, the maximum crack width increased to 0.5 mm. Pronounced cracking occurred at the beam bottom at a drift ratio of 1/125, with the maximum crack width further increasing to 1.0 mm, and concrete spalling initiated at a drift ratio of 3/125. At failure, concrete spalling at the beam bottom covered an area of approximately 100 mm × 100 mm + 0.5 × 100 mm × 200 mm.

For TB1, a horizontal crack approximately 270 mm long appeared at a drift ratio of 1/500, when cracks had already penetrated the slab section, with a maximum crack width of 0.1 mm. At a drift ratio of 3/1000, cracks penetrated the beam section and inclined cracks developed, with the maximum crack width increasing to 0.2 mm. Although pronounced cracking occurred at the beam bottom at a drift ratio of 1/125, with the maximum crack width reaching 0.5 mm, the crack distribution was less extensive than that of TB0. Concrete spalling initiated at a drift ratio of 3/125. At failure, concrete spalling at the beam bottom covered an approximately triangular region, with an estimated area of 0.5 × 200 mm × 300 mm.

For TB2, a horizontal crack approximately 300 mm long first appeared at a drift ratio of 1/1000, with a maximum crack width of 0.2 mm. Cracks penetrated the beam section at a drift ratio of 1/500, accompanied by inclined cracks and slab cracks, with the maximum crack width increasing to 0.3 mm. Pronounced beam-bottom cracking occurred at a drift ratio of 3/250, with the maximum crack width reaching 1.0 mm. Concrete spalling initiated at a drift ratio of 1/50. At failure, the concrete spalling region consisted of two areas of approximately 100 mm × 200 mm and 200 mm × 100 mm.

Overall, increasing restraint stiffness caused the beam-bottom damage region to shift upward and expand horizontally toward the beam web. To further quantify the local damage degree, the damaged area ratio was introduced based on previous damage evaluation studies [41,42], and defined as:

$$R_{\mathrm{DA}} = \frac{A_{\mathrm{D}}}{A_{\mathrm{O}}} \times 100\% \tag{1}$$

where R_{DA} is the damaged area ratio, A_{D} is the damaged concrete area, and A_{O} is the observation area. Since no obvious cracking or damage was observed in the slab, A_{O} was defined as the web region within the plastic hinge zone, namely a 400 mm × 500 mm region measured from the beam bottom. Based on the observed concrete spalling area A_{D}, the R_{DA} values of TB0, TB1, and TB2 were 10%, 15%, and 20%, respectively. This result indicates that increasing restraint stiffness aggravated local damage concentration in the beam web.

3.2 Hysteretic responses and backbone curves

Fig. 6 shows the hysteretic responses of the specimens. All specimens exhibited evident asymmetric behavior between the positive and negative loading directions. Under negative loading, the slab reinforcement was subjected to tension and contributed to load resistance, resulting in generally higher peak lateral loads than those under positive loading. The displacement corresponding to the peak point was comparable in the two loading directions. However, after the peak point was reached, the post-peak degradation behavior differed, with more gradual strength degradation under negative loading than under positive loading.

To quantify the influence of axial restraint on load-carrying capacity, the overstrength ratio Ω was defined as follows:

$$\Omega = \frac{F_{\max,k} - F_{\max,k=0}}{F_{\max,k=0}} \tag{2}$$

where $F_{\max,k}$ represents the lateral capacity corresponding to the axial restraint stiffness K_r, and $F_{\max,k=0}$ denotes the lateral capacity under the unrestrained condition.

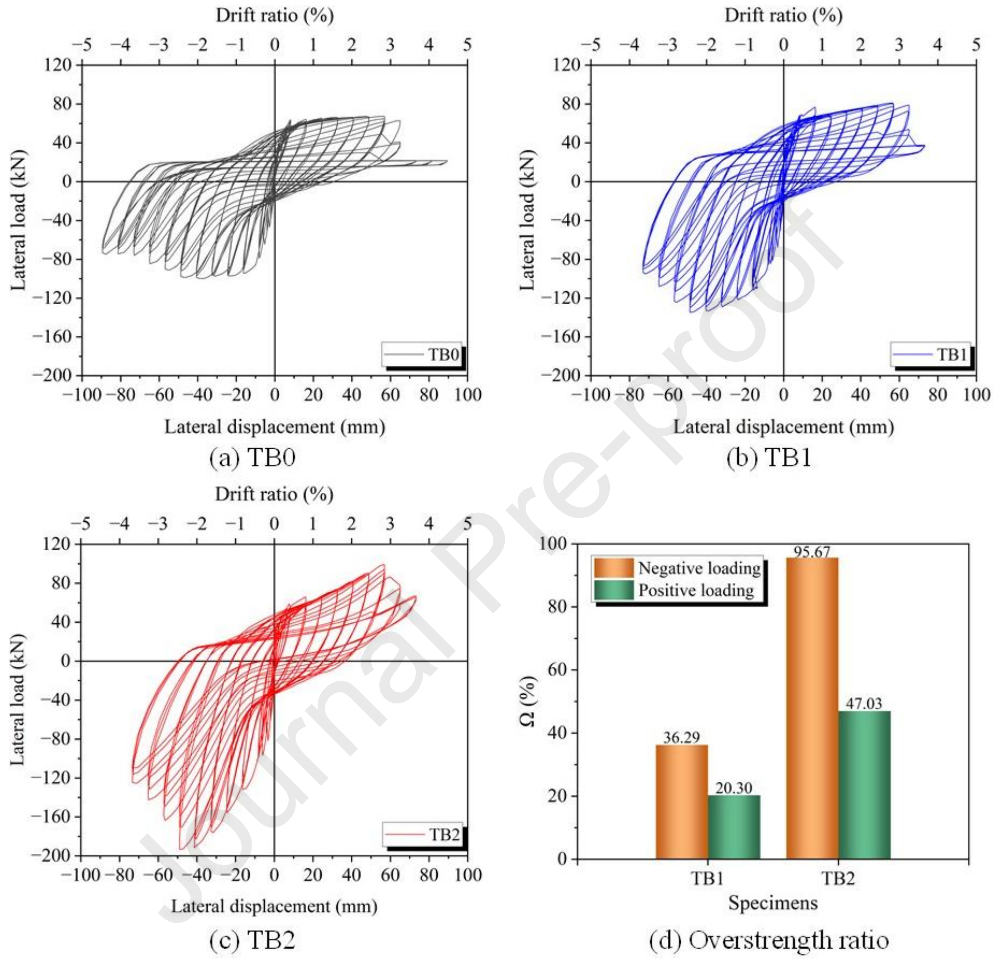

Fig. 6. Comparison of hysteresis curves

As shown in Fig. 6(d), the peak lateral load in both loading directions increased with increasing restraint stiffness, indicating that restraint stiffness had a significant influence on the flexural behavior of the specimens under cyclic loading. The overstrength ratio increased more markedly under negative loading than under positive loading, reaching 96% and 47%, respectively. This asymmetric overstrength was mainly attributed to the different role of the slab in the two loading directions. Under negative loading, the tensile force developed in the slab reinforcement provided an additional contribution to the flexural resistance. Meanwhile, the restraint-induced axial compression further enhanced the flexural capacity of the beam. As a result, the restrained specimens exhibited a more pronounced strength increase under negative loading. By contrast, under positive loading, the slab flange was mainly in compression, which enlarged the compression zone and improved the compressive resistance, but its direct contribution to the tensile force component of flexural resistance was less significant than that of the slab reinforcement under negative loading. Therefore, the overstrength ratio under positive loading was lower than that under negative loading.

Moreover, the maximum beam overstrength ratio Ω reached 96%, substantially exceeding the column-to-beam flexural strength amplification factors of approximately 20%–30% specified in seismic design codes [27–31]. This indicates that restraint-induced beam overstrength may exceed the design reserve assumed in the intended strong-column–weak-beam hierarchy and lead to strong-beam effects. Therefore, the additional flexural capacity generated by slab action and restraint-induced axial compression should be considered when evaluating the moment demands at connected column ends and the force demands on beam-column joints. This observation also highlights the need to evaluate restrained T-shaped beams as compression-bending members for flexural capacity assessment, as further discussed in Section 4.5.

To analyze the evolution of the load response at different loading stages, the characteristic points of the backbone curves were determined using Park's method [43]. Fig. 7 shows the backbone curves and the corresponding characteristic points of each specimen in the positive and negative loading directions.

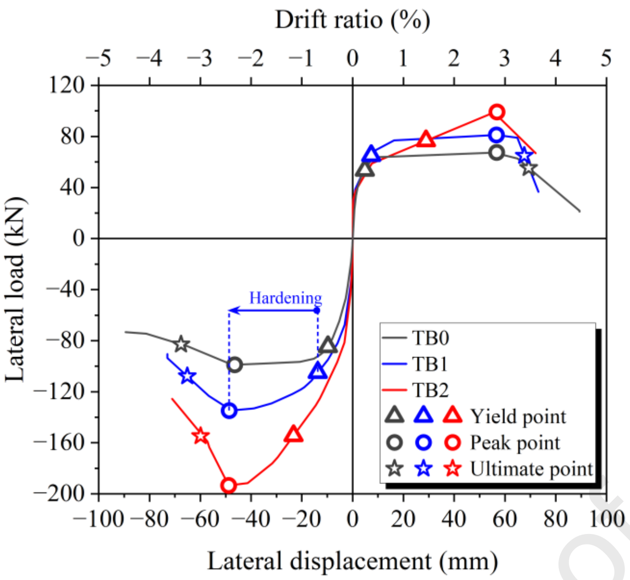

Fig. 7. Comparison of backbone curves

As shown in Fig. 7, the backbone curves were generally consistent during the early loading stage. After yielding, however, clear differences developed among the specimens. This behavior can be attributed to the interaction between beam elongation and axial restraint. During post-yield loading, the axial elongation continued to increase, and the axial restraint system converted this elongation into progressively increasing axial compression. As a result, the flexural resistance was continuously enhanced instead of developing a distinct yield plateau [7]. Moreover, higher restraint stiffness increased the rate at which beam elongation generated axial compression and led to a larger maximum restraint-induced axial compression during post-yield loading, resulting in a steeper post-yield hardening branch.

In addition, the backbone curves exhibited an evident asymmetric response between the positive and negative loading directions owing to slab action. As the restraint stiffness increased, the difference between the positive and negative peak lateral loads became more pronounced. At restraint stiffnesses of 0, 30, and 99 kN/mm, the negative peak lateral loads were 104, 135, and 193 kN, respectively, which were 49%, 66%, and 95% higher than the corresponding positive peak lateral loads. The specimens also exhibited more gradual post-peak strength degradation under negative loading than under positive loading. This asymmetry can be explained by the different mechanical roles of the slab under opposite loading directions. Under negative loading, the slab reinforcement was subjected to tension and provided additional longitudinal tensile resistance, thereby enhancing the sectional flexural capacity and contributing to a more stable post-peak response. By contrast, under positive loading, the slab mainly acted as a compression flange, and the post-peak response was more sensitive to concrete crushing in the compression zone.

3.3 Stiffness degradation and cumulative energy dissipation

The lateral stiffness of each specimen at loading level i was calculated separately for the positive and negative loading directions as follows:

$$K^{\pm}_{L,i} = \frac{F^{\pm}_{L,i}}{\Delta^{\pm}_{L,i}} \tag{3}$$

where $K^{\pm}_{L,i}$ denotes the lateral stiffness at loading level i; the superscripts + and − indicate the positive and negative loading directions, respectively; $F^{\pm}_{L,i}$ is the maximum lateral load in the corresponding loading direction at loading level i; and $\Delta^{\pm}_{L,i}$ is the corresponding maximum lateral displacement.

Fig. 8 illustrates the lateral stiffness degradation of each specimen during loading. In both the positive and negative loading directions, the stiffness initially decreased rapidly, followed by a gradual reduction in the degradation rate. Throughout the loading process, the restrained specimens exhibited higher lateral stiffness than the unrestrained specimen, and the stiffness generally increased with increasing restraint stiffness. This improvement can be attributed to the restraint-induced axial compression generated by restrained beam elongation, which limited crack opening and promoted post-yield hardening of the specimens.

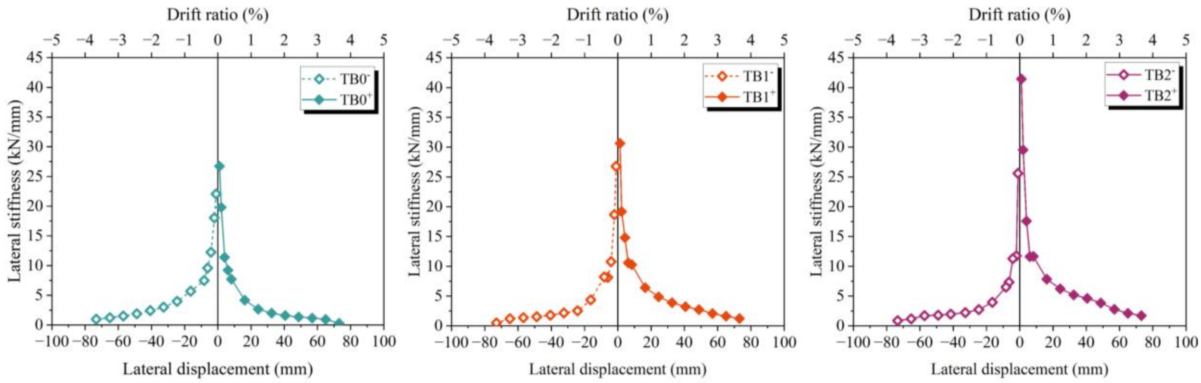

(a) TB0 (b) TB1 (c) TB2

Fig. 8. Comparison of lateral stiffness

Fig. 9 shows the cumulative energy dissipation of each specimen. With increasing restraint stiffness, the cumulative energy dissipation at the same loading level increased, and the increment in cumulative energy dissipation between adjacent loading levels also became larger. Based on the loading displacement corresponding to the earliest specimen failure, the cumulative energy dissipation of TB0, TB1, and TB2 at the end of loading was 30,304, 36,763, and 43,098 kN·mm, respectively. When the restraint stiffness increased from 0 to 30 and 99 kN/mm, the cumulative energy dissipation increased by 21% and 42%, respectively, indicating that axial restraint enhanced the energy dissipation capacity of the specimens.

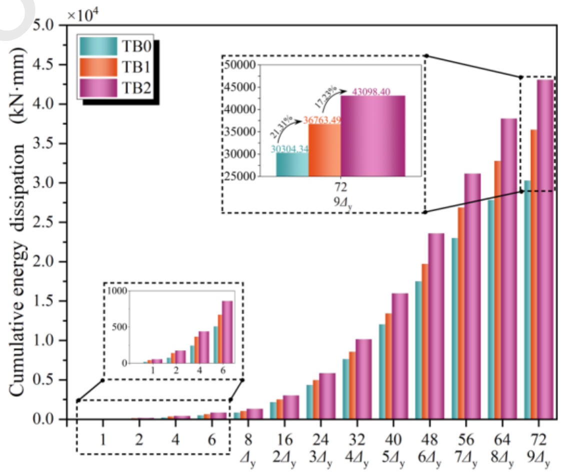

Fig. 9. Cumulative energy dissipation of the specimens

3.4 Axial elongation

During the early loading stage, axial elongation increased progressively and remained approximately symmetric in the positive and negative loading directions. As restraint stiffness increased, the peak-point axial elongation decreased in both loading directions. For TB0, TB1, and TB2, the peak-point axial elongations were 9.16, 7.26, and 5.81 mm under positive loading, respectively, and 7.78, 7.15, and 5.75 mm under negative loading, respectively. In the later loading stage, especially after the peak point was reached, the axial elongation response became asymmetric. Under positive loading, the elongation continued to increase with further loading, whereas under negative loading, it generally stabilized and fluctuated within a range of approximately 2 mm. This asymmetry was mainly attributed to the different compression regions in the two loading directions: concrete crushing occurred at the beam bottom under negative loading, limiting further elongation development, whereas slab action prevented obvious concrete crushing in the flange region under positive loading, allowing axial elongation to continue increasing.

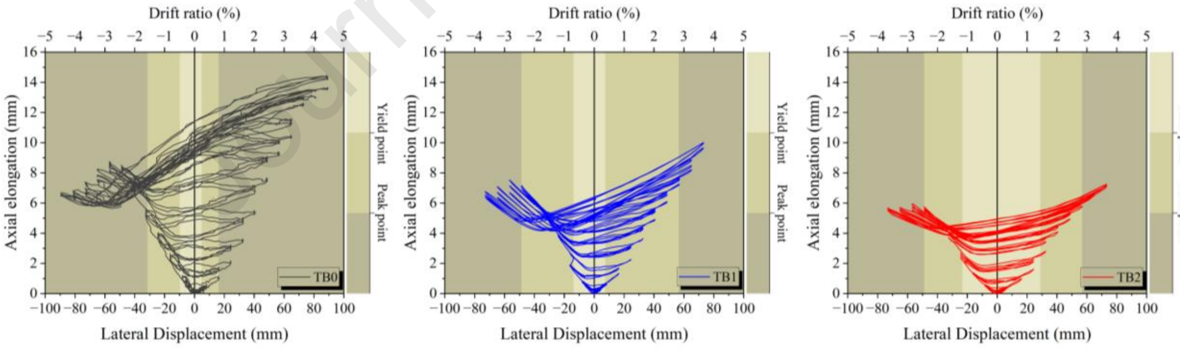

(a) TB0 (b) TB1 (c) TB2

Fig. 10. Axial elongation of specimens

Under cyclic loading, the axial elongation of RC members can be decomposed into recoverable geometric elongation and unrecoverable residual elongation [8–9]. Fig. 11 illustrates the decomposition of the total elongation at the *i*-th loading level into recoverable geometric and unrecoverable residual components. Points A–D denote the start of the loading level, the maximum displacement in the positive direction, the maximum displacement in the negative direction, and the end of the loading level, respectively. $\Delta_{TEmax,i}$ represents the maximum attained total elongation, $\Delta_{RE,i}$ represents the residual elongation measured at Point D, and $\Delta_{GE,i}^{+}$ and $\Delta_{GE,i}^{-}$ are the geometric elongation components under positive and negative loading, respectively.

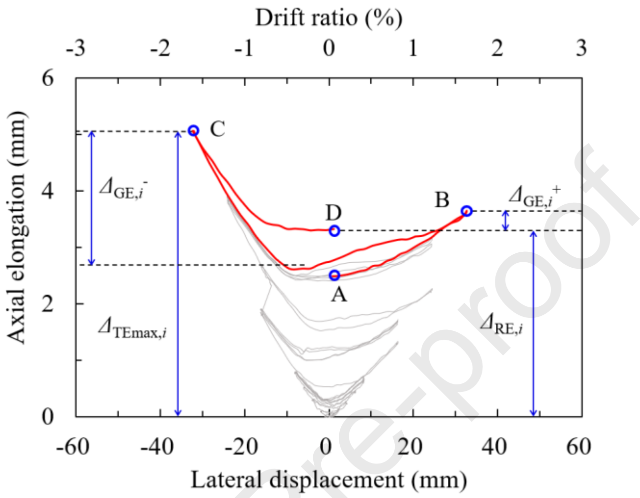

Fig. 11. Composition of axial elongation

To characterize the development of plastic elongation within the total axial elongation, the residual elongation ratio R_{re} was defined based on the elongation components shown in Fig. 11, as expressed in Eq. (4):

$$R_{re} = \frac{\Delta_{RE,\,i}}{\Delta_{TEmax,\,i}} \tag{4}$$

where $\Delta_{RE,i}$ and $\Delta_{TEmax,i}$ denote the residual axial elongation and the maximum axial elongation at the i-th loading level, respectively.

Based on Eq. (4), Fig. 12 shows the residual elongation ratio R_{re} of each specimen at each loading level. During the early loading stage, R_{re} exhibited unstable fluctuations. This was mainly because the axial elongation was relatively small before yielding, making the calculated residual elongation ratio more sensitive to specimen-related uncertainties, such as minor geometric imperfections and fabrication defects, as well as test-related uncertainties, such as measurement noise and installation errors. After the loading displacement reached a certain level, however, R_{re} generally first increased and then decreased. By examining Fig. 12 together with Fig. 7, it can be observed that the transition from unstable fluctuations to a more stable trend approximately coincided with the yield point of each specimen. After yielding, the plastic deformation region and damage concentration zone gradually stabilized, and the relative influence of these uncertainties diminished. Therefore, the post-yield trend of R_{re} is considered more representative for evaluating the development of residual elongation.

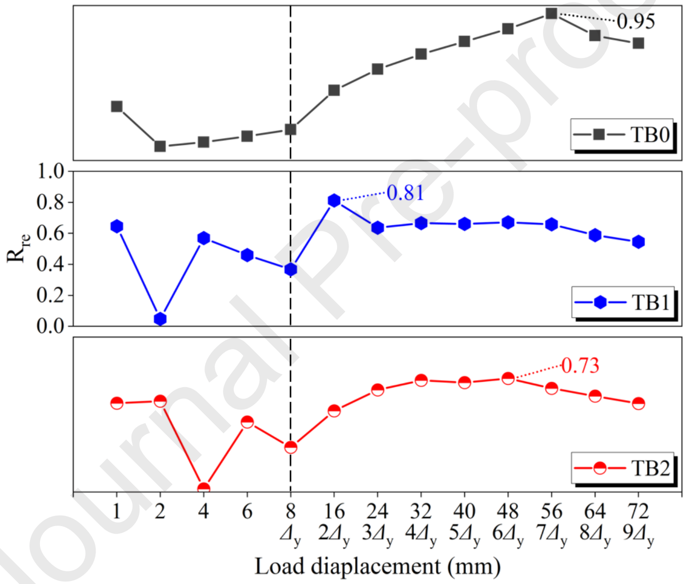

Fig. 12. Evolution of residual elongation ratio

From yielding to the peak point, plastic deformation accumulated in the yielded reinforcement under increasing external load, leading to an increase in R_{re}. This indicates that residual elongation became increasingly dominant in the total axial elongation after yielding and extensive flexural cracking. After the peak point was reached, progressive damage in the reinforcement and concrete, together with degradation at the beam-base interface, increased the proportion of recoverable axial elongation. As a result, R_{re} gradually decreased. This apparent recoverability should not be interpreted as spontaneous recovery of the specimen, but rather as a passive deformation response governed by external loading and degraded structural resistance.

In addition, as the restraint stiffness increased from 0 to 30 and 99 kN/mm, the maximum residual elongation ratio decreased from 0.95 to 0.81 and 0.73, corresponding to reductions of 15% and 23%, respectively. This suggests that the residual elongation component was more sensitive to axial restraint than the recoverable elongation component, because restraint-induced axial compression mainly suppressed residual crack opening and unrecoverable bond-slip deformation, while the recoverable component was more closely related to elastic deformation under the applied loading [9].

From an engineering perspective, a lower R_{re} indicates that a smaller proportion of beam elongation remains after unloading, suggesting that axial restraint reduces the residual component. However, this reduction is achieved through stronger restraint from the surrounding frame system, which may induce larger axial compression and transfer additional force demands to adjacent columns and beam–column joints. Therefore, a lower R_{re} should not be interpreted simply as a reduced demand on the surrounding structural members. In addition, the post-peak decrease in R_{re} should not be regarded as improved recoverability. During the post-peak stage, the specimens experienced progressive damage, including crack widening, concrete spalling, and strength degradation. Although axial restraint reduced the residual elongation proportion, the accompanying local damage accumulation may still impair the post-earthquake repairability of the beam. The relationships among axial restraint, residual elongation recovery, damage accumulation, and post-earthquake repairability require further investigation.

3.5 Axial compression analysis

Fig. 13 shows the restraint-induced axial compression responses of TB1 and TB2 during loading. In the early loading stage, the axial compression increased approximately symmetrically in the positive and negative loading directions. After the peak point was reached, pronounced asymmetry developed: the axial compression in the positive direction continued to increase with further loading, whereas that in the negative direction began to decrease. Increasing restraint stiffness led to higher restraint-induced axial compression.

At the peak points, the axial compression of TB1 was 221 kN and 210 kN in the positive and negative loading directions, respectively. For TB2, the corresponding values increased to 576 kN and 563 kN, representing increases of 161% and 168%, respectively, as the restraint stiffness increased from 30 to 99 kN/mm. Together with the elongation results shown in Fig. 10, these results indicate that a higher restraint stiffness substantially increased the restraint-induced axial compression, although the corresponding axial elongation was reduced.

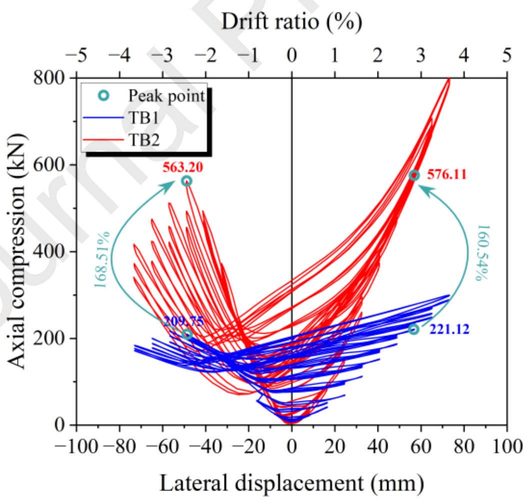

Fig. 13. Restraint-induced axial compression responses

3.6 Comprehensive analysis

Fig. 14 presents a radar chart of the normalized mechanical indicators based on the experimental results. For each indicator, the value of the unrestrained specimen TB0 was taken as the reference value of 1.0, and the corresponding values of TB1 and TB2 were normalized relative to TB0. The peak lateral loads in the positive and negative directions and the cumulative energy dissipation mainly reflect the strength and energy-dissipation capacity of the specimens, whereas the peak-point axial elongations and residual elongation ratio represent beam growth and residual deformation demands. The stiffness retention ratio was defined as the ratio of the lateral stiffness at failure to the initial lateral stiffness. Therefore, a larger value indicates better stiffness retention and slower stiffness degradation during cyclic loading.

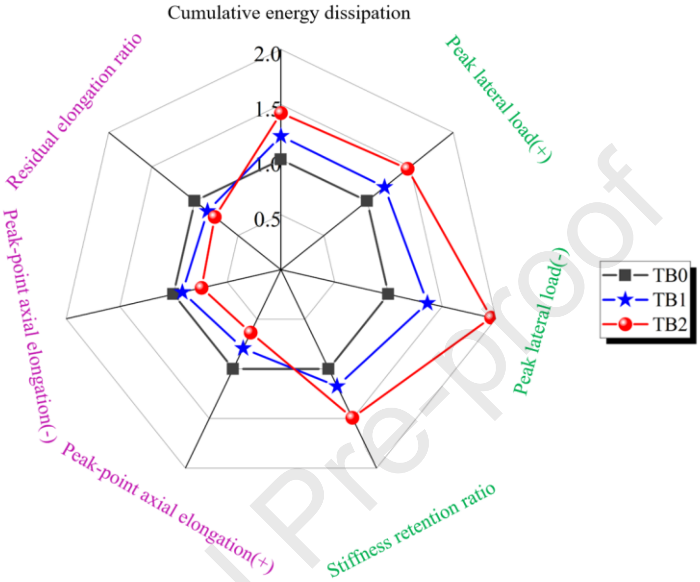

Fig. 14. Radar chart of normalized mechanical performance relative to unrestrained specimen TB0

As shown in Fig. 14, increasing restraint stiffness generally increased the normalized peak lateral loads and cumulative energy dissipation, indicating enhanced lateral resistance and energy-dissipation capacity. The normalized stiffness retention ratio also increased, which was consistent with the observation in Fig. 8 that axial restraint increased the specimen stiffness throughout the loading process and slowed stiffness degradation toward failure. Meanwhile, the normalized peak-point axial elongations and residual elongation ratio decreased, indicating that axial restraint helped limit beam growth and the residual component of elongation. Overall, the radar chart provides an intuitive visualization of the influence of axial restraint on the cyclic performance of T-shaped RC beams, including strength enhancement, energy dissipation, stiffness retention, beam growth, and residual deformation, thereby providing useful references for seismic design and future studies on restrained RC beams.

4. Numerical simulation

4.1 Material constitutive models and mesh discretization

A finite-element model of each tested specimen was established in ABAQUS. In the model, concrete and reinforcing steel were treated as homogeneous materials at the macroscopic scale. The concrete was modeled using the concrete damaged plasticity (CDP) model. The reinforcement was embedded in the concrete to define its geometric location, while the bond-slip effect between reinforcement and concrete was considered through the user subroutine-based reinforcement constitutive model proposed in [44]. The reinforcing steel was assumed to follow the von Mises yield criterion. The tensile and compressive constitutive relationships for concrete specified in the code [38] were adopted. The elastic modulus of concrete was taken as 30740 N/mm², and Poisson's ratio was taken as 0.2. The main CDP parameters adopted in ABAQUS are summarized in Table 3.

Table 3

Constitutive model parameters of concrete

Dilation angle ψ	Eccentricity e	Biaxial-to-uniaxial compressive yield stress ratio f_{b0}/f_{c0}	Shape factor K_c	Viscosity parameter μ
30	0.1	1.16	0.667	0.0005

The tensile constitutive relationship of concrete is expressed as follows:

$$\sigma = (1 - d_t) E_c \varepsilon \tag{5}$$

$$d_t = \begin{cases} 1 - \rho_t \left(1.2 - 0.2x^5\right) & x \le 1 \\ 1 - \dfrac{\rho_t}{\alpha_t (x-1)^{1.7} + x} & x > 1 \end{cases} \tag{6}$$

$$x = \frac{\varepsilon}{\varepsilon_{t,r}} \tag{7}$$

$$\rho_{\mathrm{t}} = \frac{f_{\mathrm{t,\,r}}}{E_{\mathrm{c}}\varepsilon_{\mathrm{t,\,r}}} \tag{8}$$

The compressive constitutive relationship of concrete is expressed as follows:

$$\sigma = (1 - d_{\mathrm{c}})E_{\mathrm{c}}\varepsilon \tag{9}$$

$$d_{\mathrm{c}} = \begin{cases} 1 - \dfrac{\rho_{\mathrm{c}} n}{n - 1 + x^{\mathrm{n}}} & x \le 1 \\ 1 - \dfrac{\rho_{\mathrm{c}}}{\alpha_{\mathrm{c}}(x-1)^2 + x} & x > 1 \end{cases} \tag{10}$$

$$\rho_{\mathrm{c}} = \frac{f_{\mathrm{c,\,r}}}{E_{\mathrm{c}}\varepsilon_{\mathrm{c,\,r}}} \tag{11}$$

$$n = \frac{E_{\mathrm{c}}\varepsilon_{\mathrm{c,\,r}}}{E_{\mathrm{c}}\varepsilon_{\mathrm{c,\,r}} - f_{\mathrm{c,\,r}}} \tag{12}$$

$$x = \frac{\varepsilon}{\varepsilon_{\mathrm{c,\,r}}} \tag{13}$$

where σ and ε denote stress and strain, respectively; E_c is the elastic modulus of concrete, d_t and d_c are the tensile and compressive damage evolution parameters, respectively; α_t and α_c are the parameters controlling the descending branches of the tensile and compressive stress-strain curves, respectively; $f_{t,r}$ and $\varepsilon_{t,r}$ are the representative tensile strength and the corresponding peak tensile strain, respectively; $f_{c,r}$ and $\varepsilon_{c,r}$ are the representative compressive strength and the corresponding peak compressive strain, respectively.

The mesh size was selected with reference to previous studies on RC members, in which mesh sizes within approximately 0.02–0.06 times the longest member dimension were commonly adopted to balance computational efficiency and accuracy [37, 45–47]. Based on these studies, mesh sizes of 70 mm, 50 mm, 70 mm, 30 mm, and 100 mm were adopted for the slab reinforcement parallel to the beam axis, slab reinforcement perpendicular to the beam axis, beam longitudinal reinforcement, beam stirrups, and concrete elements, respectively. The adopted mesh configuration provided stable numerical convergence and reasonably captured the global hysteretic response and axial elongation behavior of the specimens.

4.2 Finite-element model setup

Fig. 15 shows the finite-element model configuration. After the concrete, reinforcement, and loading plate components were created in ABAQUS, they were assembled and meshed. The concrete was modeled using C3D8R solid elements, the reinforcement was modeled using T3D2 truss elements, and the loading plate was modeled using S4R shell elements. The loading plate was tied to the top surface of the concrete. According to the locations of the steel-rod holes in the test specimens, two reference points, RP-1 and RP-2, were defined at the model base. The extended parts of the loading plate were connected to RP-1 and RP-2 using spring elements, with stiffness values consistent with the experimental restraint stiffnesses. The model base was fixed, and displacement loading was applied at the top of the specimen following the experimental loading protocol.

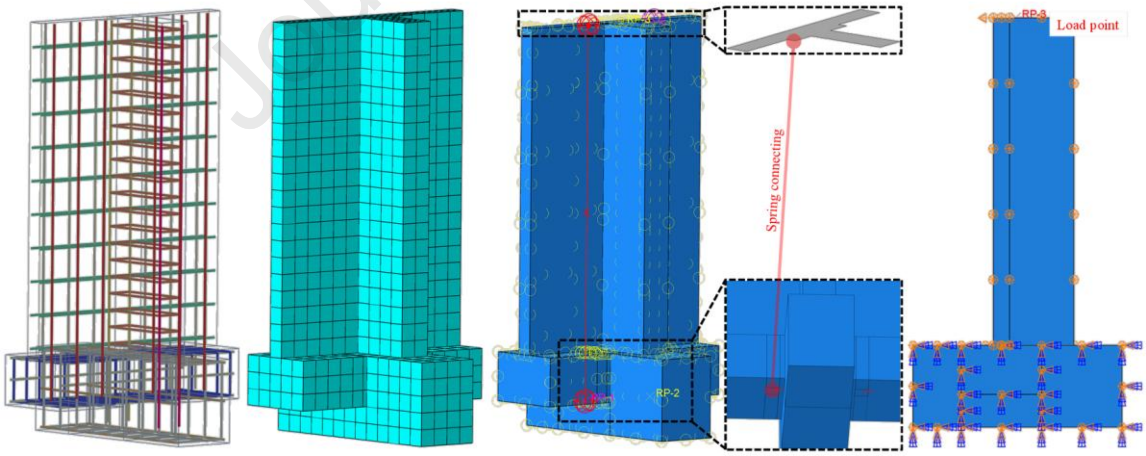

(a) Model assembly (b) Mesh configuration (c) Interaction settings (d) Boundary conditions

Fig. 15. Finite-element model setup

4.3 Model validation

As shown in Fig. 16, the numerical results agreed reasonably well with the experimental results in terms of global cyclic response. The simulated hysteresis curves captured the main response characteristics of the specimens, including the asymmetric behavior between the positive and negative loading directions. The comparison of backbone curves further shows that the finite-element model reasonably reproduced the envelope response and peak lateral loads. In addition, the simulated stiffness degradation curves followed the experimental trends, indicating that the model could capture the reduction in lateral stiffness during cyclic loading.

The axial elongation responses obtained from the numerical model were also generally consistent with the experimental observations, including the asymmetric development of axial elongation in the positive and negative loading directions. Some discrepancies were observed in the unloading branches after the specimens reached their peak lateral loads. This was mainly because concrete crushing, crack propagation, crack opening and closure, bond-slip-related residual deformation, and local spalling during the strength-degradation stage exhibited inherent discreteness and randomness, making the unloading stiffness and residual deformation difficult to reproduce accurately. Nevertheless, the model reasonably captured the peak lateral loads, backbone curves, stiffness degradation trends, peak-point axial elongations, and general damage evolution. Therefore, it was considered suitable for the subsequent global response and damage analyses and for providing supplementary information on local stress, strain, and damage development that was not directly measured in the tests.

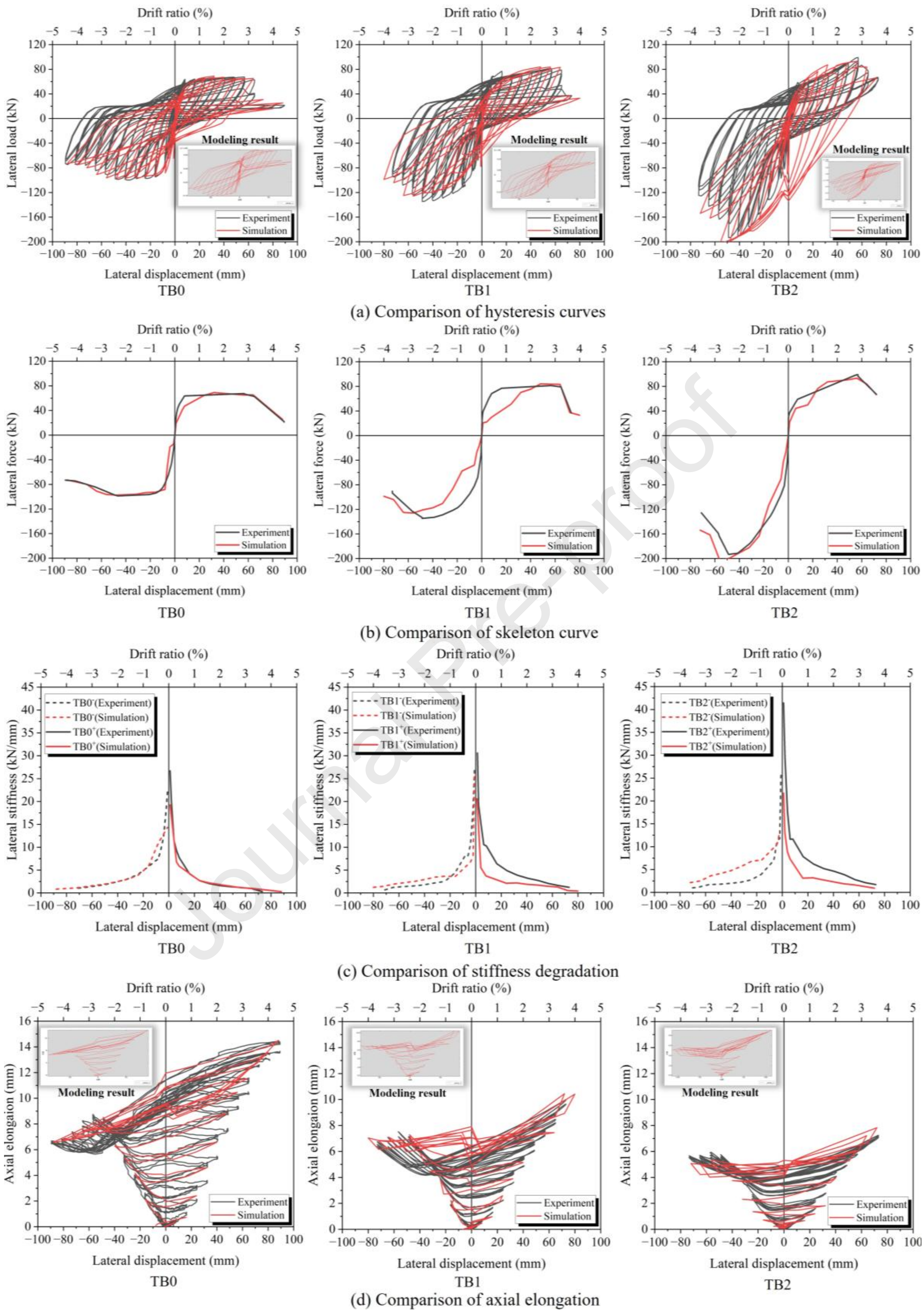

Fig. 16. Comparison between numerical and experimental results

After the specimens reached their peak lateral loads, significant damage developed and the load-carrying capacity began to degrade. To further evaluate the predictive accuracy of the numerical model, the peak lateral loads in the positive and negative loading directions and the corresponding peak-point axial elongations were compared, as summarized in Table 4.

Table 4

Comparison between experimental and simulated peak lateral loads and peak-point axial elongations

Specimen	Peak lateral load						Peak-point axial elongation					
	Positive			Negative			Positive			Negative		
	Exp. (kN)	Sim. (kN)	Error (%)	Exp. (kN)	Sim. (kN)	Error (%)	Exp. (mm)	Sim. (mm)	Error (%)	Exp. (mm)	Sim. (mm)	Error (%)
TB_0	67.53	69.14	2.33	103.50	96.17	7.08	9.16	7.67	16.27	7.78	7.45	4.24
TB_1	81.20	83.75	3.14	134.70	120.76	10.35	7.26	7.89	8.68	7.15	7.29	1.96
TB_2	99.30	93.16	6.18	193.30	199.37	3.14	5.81	6.08	4.65	5.75	4.87	15.30

As shown in Table 4, the maximum errors in peak lateral load and peak-point axial elongation were less than 11% and 17%, respectively, indicating that the numerical model reasonably captured the force and deformation responses of the specimens under cyclic loading.

After validating the global response, the equivalent plastic strain in concrete and the equivalent stress in reinforcement were further examined to interpret the local strain and stress development. As shown in Fig. 17, the equivalent plastic strain in concrete was mainly concentrated at the beam bottom, and its distribution range was generally consistent with the observed failure region. The reinforcement stress was also mainly concentrated at the beam bottom, while most of the slab reinforcement exhibited a relatively uniform stress distribution across the section width. At the end of loading, TB1 and TB2 showed similar peak reinforcement stresses and stress distributions. Although the peak reinforcement stress in TB0 was lower, its high-stress region was noticeably wider than those of the restrained specimens. This indicates that the wider high-stress region in the reinforcement was associated with more extensive tensile strain development, thereby contributing to the more pronounced axial elongation observed in TB0.

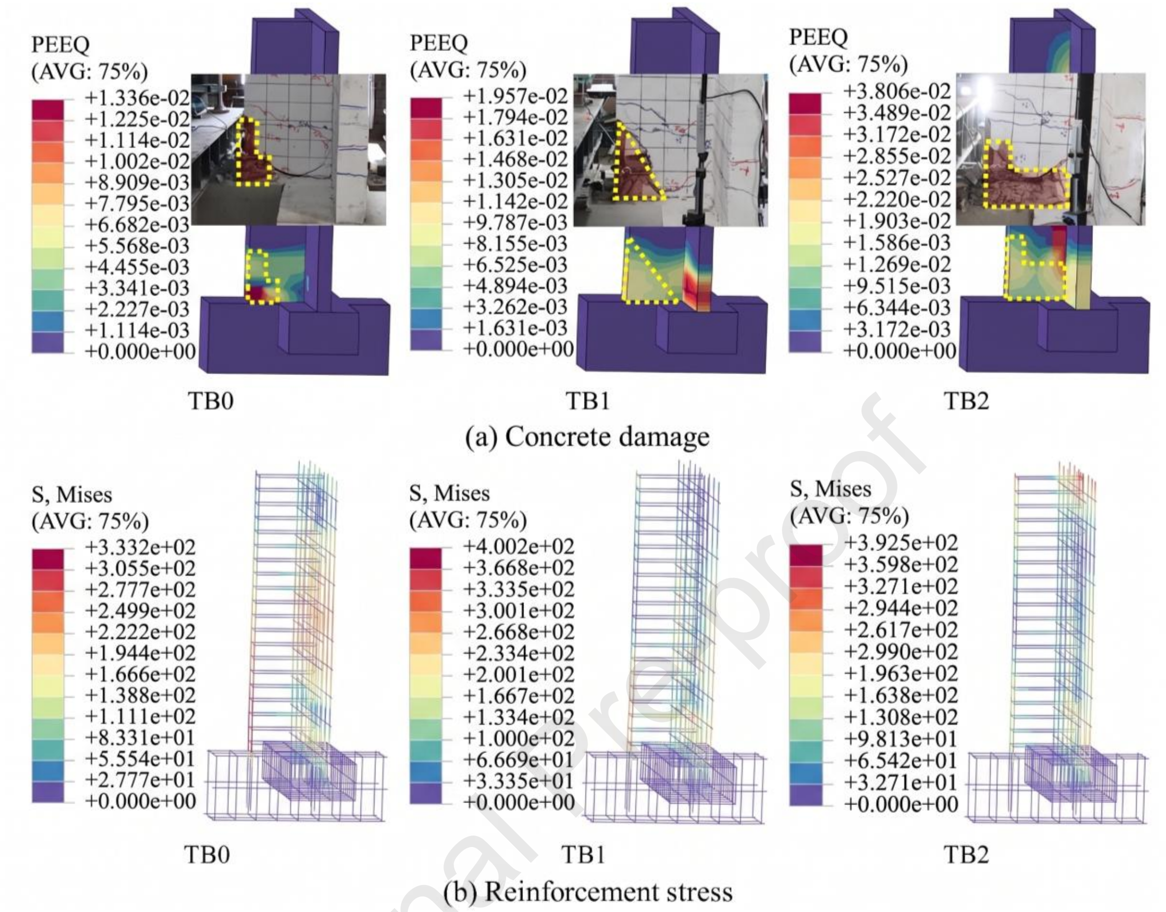

Fig. 17. Stress and strain distributions of reinforcement and concrete

4.4 Damage distribution

Based on the concrete constitutive relationships used in the model, Fig. 18 separately presents the elements in which tensile and compressive damage exceeded the predefined damage threshold.

The damage distribution was generally consistent with the stress state of the specimens, with damage severity decreasing from the beam bottom toward the upper part of the section. With increasing restraint stiffness, both tensile and compressive concrete damage became more severe, suggesting that axial restraint promoted more extensive plastic development and damage evolution in the concrete.

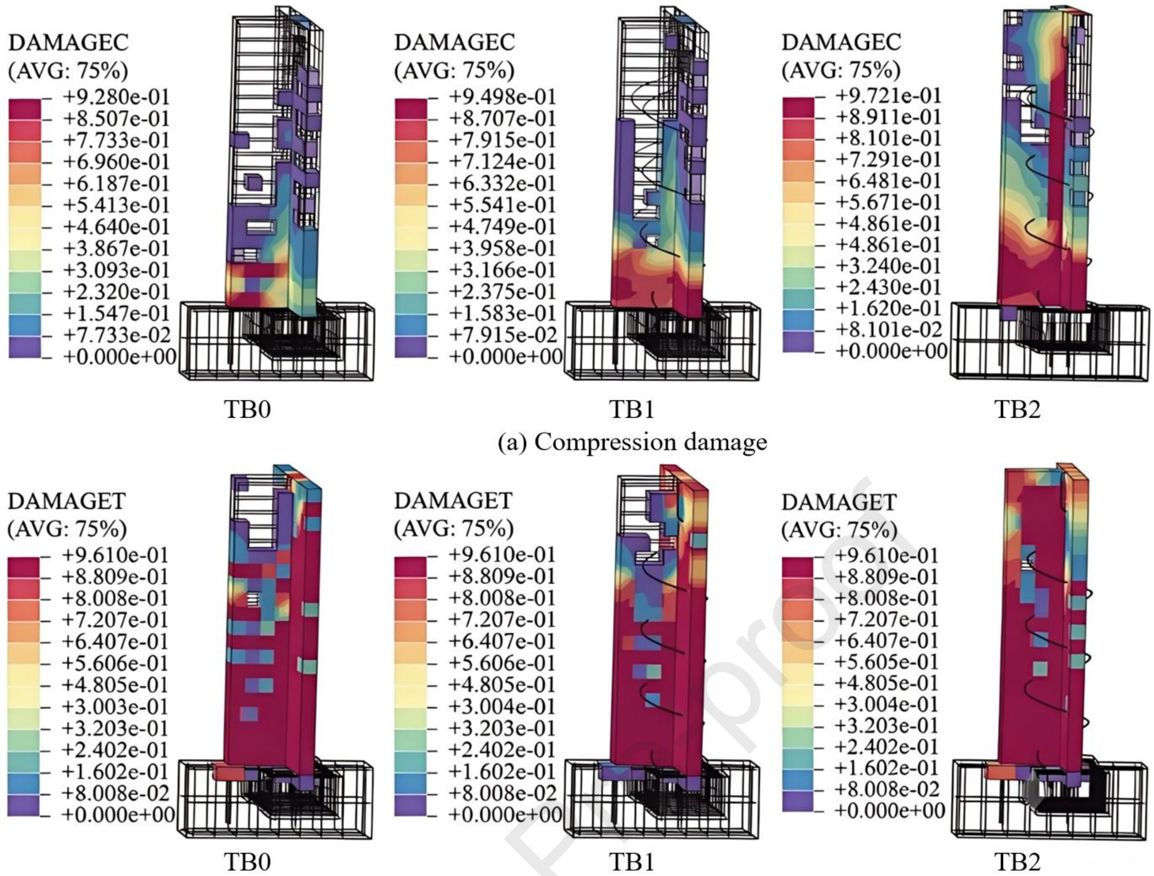

(a) Compression damage

(b) Tension damage

Fig. 18. Damage distribution of concrete

In the RC specimens, damage was most severe in the plastic hinge region. To evaluate the combined tensile and compressive damage in the plastic hinge region, the top and bottom nodes of the plastic hinge were selected for analysis. The scalar stiffness degradation variable SDEG in ABAQUS was used as the damage index, as illustrated in Fig. 19.

The results show that stiffness degradation along the section height exhibited an approximately symmetric distribution, with greater degradation generally observed at the bottom than at the top of the plastic hinge. Overall, increasing restraint stiffness led to more severe stiffness degradation in the plastic hinge region, while reducing the difference between the top and bottom. In addition, the fluctuations in SDEG gradually diminished with increasing restraint stiffness, especially at the bottom of the plastic hinge. This trend is consistent with the previous analysis and can be attributed to the more fully developed concrete damage at the beam bottom.

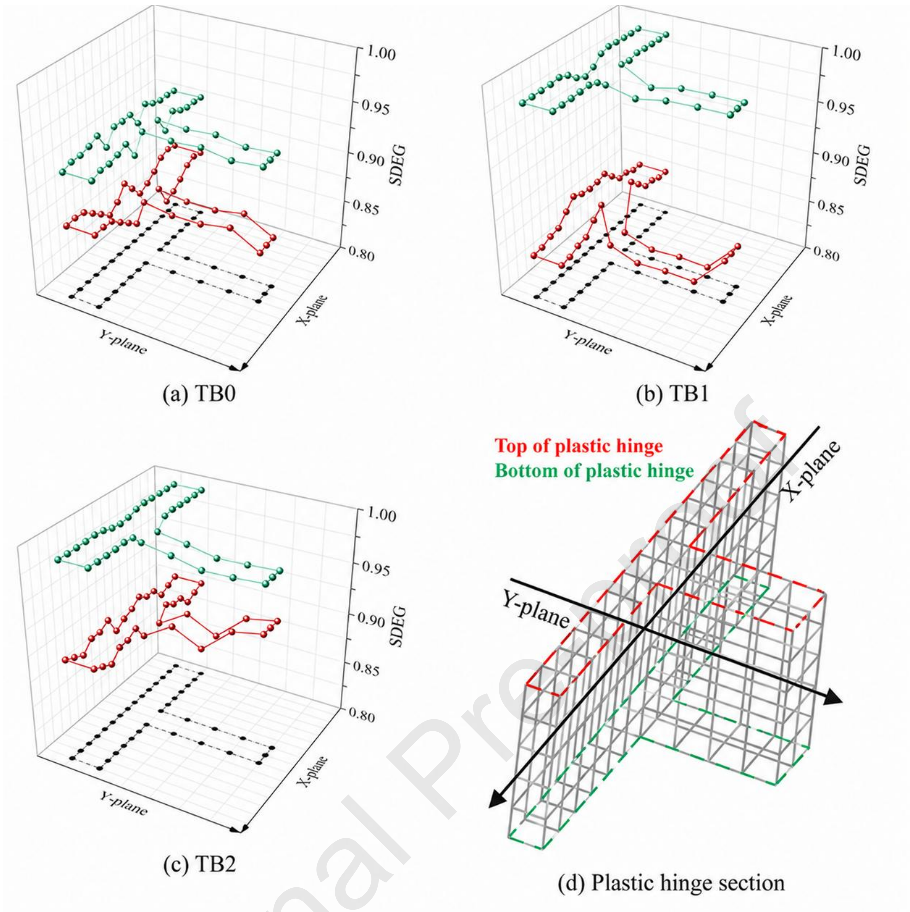

Fig. 19. Damage distribution of plastic hinge

4.5 Constant-axial-compression analysis

Since restraint-induced axial compression significantly enhances the flexural capacity of restrained beams, its influence should be considered in flexural capacity design. To examine whether restrained T-shaped beams can be simplified as compression-bending members for capacity assessment, additional simulations were conducted under constant axial compression.

As shown in Fig. 20, the average values of the restraint-induced axial compression measured at the positive and negative peak lateral loads of TB1 and TB2 were applied as constant external axial compressions in the simulations. In the tests, the specimens were subjected to constant axial-restraint stiffness, and the restraint-induced axial compression varied with beam elongation during cyclic loading. Compared with these experimental responses, the simulations with constant axial compression showed higher initial stiffness in the hysteresis curves, while the post-peak flexural capacity degraded more rapidly after the peak was reached. These differences indicate that the constant-axial-compression simplification cannot fully reproduce the cyclic response of specimens tested under constant axial-restraint stiffness, where the restraint-induced axial compression varied with beam elongation.

Nevertheless, the peak lateral loads obtained from the constant-axial-compression simulations were close to the experimental results in both positive and negative loading directions. Since the specimens failed primarily in flexure, these peak lateral loads correspond to the flexural capacities of the specimens. Combined with the results shown in Fig. 13, this suggests that although the restraint-induced axial compression varied during cyclic loading, the flexural capacity was mainly governed by the axial compression level developed near the peak response. Therefore, for flexural capacity design, restrained T-shaped beams may be evaluated as compression-bending members by using the maximum restraint-induced axial compression as the applied external axial compression.

However, this simplification is mainly applicable to flexure-dominated restrained T-shaped RC beams within the investigated range of the restraint coefficient κ, i.e., 0.00–0.03, and should be used primarily for capacity assessment rather than for direct prediction of the full hysteretic response. This is because beam axial elongation is mainly associated with flexural crack opening, tensile plastic strain accumulation, and bond slip of longitudinal reinforcement, and is therefore more pronounced in flexure-dominated specimens [9]. For specimens governed by shear failure or pronounced flexural-shear interaction, the elongation mechanism, restraint-induced axial compression development, and failure mode may differ. Therefore, its applicability to these cases, as well as to restrained beams with restraint coefficients larger than the investigated range, requires further validation.

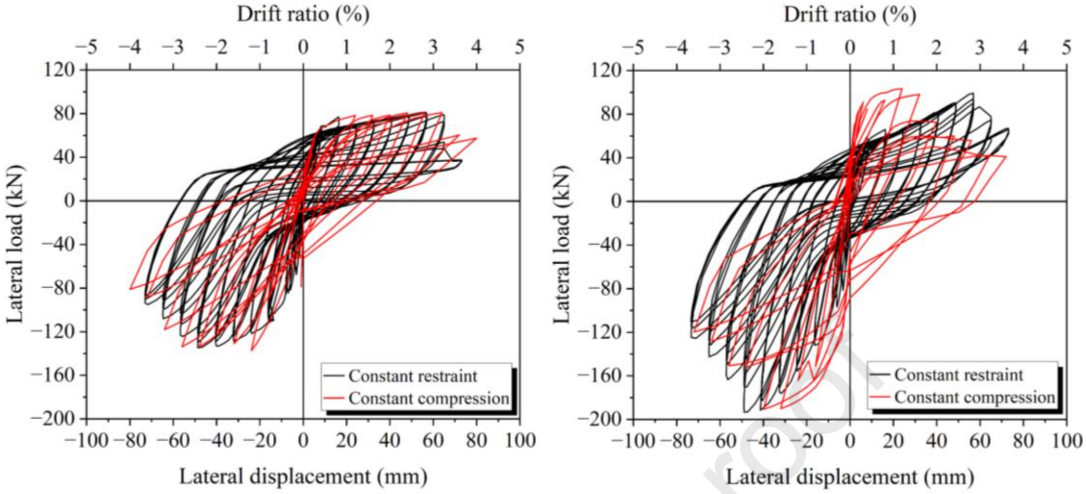

(a) TB1 (b) TB2

Fig. 20. Comparison between experimental responses under constant axial-restraint stiffness and simulations under constant axial compression

5. Conclusion

Three full-scale T-shaped RC beam specimens were subjected to quasi-static cyclic loading to investigate their hysteretic behavior and axial elongation response, with restraint stiffness as the main variable. An ABAQUS finite-element model was developed and validated against the experimental results, and was further used to analyze the stress state, damage distribution, and flexural capacity of the restrained specimens. The main conclusions are summarized as follows:

(1) Axial restraint suppressed the development of axial elongation and changed its composition. As the restraint stiffness increased from 0 to 99 kN/mm, the peak-point axial elongation decreased from 9.16 to 5.81 mm under positive loading and from 7.78 to 5.75 mm under negative loading. Meanwhile, the maximum residual elongation ratio decreased from 0.95 to 0.73, indicating that axial restraint suppressed residual elongation more significantly than recoverable geometric elongation. The elongation response was approximately symmetric during the early loading stage but became asymmetric after the peak point owing to slab action.

(2) Axial restraint significantly increased the restraint-induced axial compression and beam overstrength. At the peak points, the restraint-induced axial compression reached 576 kN, and the maximum overstrength ratio reached 96%. These considerable levels of axial compression and overstrength may significantly increase beam-end force demands and affect force redistribution in RC frame systems, and should therefore be considered in seismic capacity design.

(3) Axial restraint caused evident post-yield hardening in the backbone curves. During post-yield loading, beam elongation was converted into progressively increasing restraint-induced axial compression, which continuously enhanced the flexural resistance instead of producing a distinct yield plateau. Higher restraint stiffness led to a steeper post-yield hardening branch. The backbone curves also showed asymmetric responses owing to slab action, with higher absolute peak lateral loads and more gradual post-peak strength degradation under negative loading because the slab reinforcement contributed to the flexural resistance in tension.

(4) Increasing restraint stiffness enhanced the lateral stiffness and cumulative energy dissipation capacity of the specimens. The restrained specimens exhibited higher lateral stiffness than the unrestrained specimen throughout loading, mainly because restraint-induced axial compression limited crack opening and promoted post-yield hardening. Compared with the unrestrained specimen, the cumulative energy dissipation increased by 21% and 42% at restraint stiffnesses of 30 and 99 kN/mm, respectively.

(5) The ABAQUS finite-element model reasonably captured the force and deformation responses of the restrained T-shaped beams. The maximum errors in peak lateral load and peak-point axial elongation were less than 11% and 17%, respectively, indicating that the model

could reproduce the main global response characteristics of the specimens.

(6) The simulated stress concentration regions were generally consistent with the observed failure zones. As restraint stiffness increased, the concrete damage region enlarged from the beam bottom toward the upper part of the section. Correspondingly, the difference in stiffness degradation between the top and bottom of the plastic hinge decreased, while the overall stiffness degradation in the plastic hinge region increased.

(7) Constant-axial-compression analyses based on the validated finite-element model showed that the flexural capacities of restrained T-shaped beams could be reasonably predicted by considering the maximum restraint-induced axial compression. Therefore, restrained T-shaped beams may be simplified as compression-bending members for flexural capacity assessment, although this simplification is not intended to reproduce the full hysteretic response under axial-restraint stiffness.

It should also be noted that only two axial restraint stiffness levels were considered in addition to the unrestrained specimen. Therefore, the systematic relationship between axial restraint stiffness and the hysteretic behavior of restrained T-shaped RC beams over a wider stiffness range still requires further investigation. The proposed compression-bending-based design simplification was developed within the scope of the present study and is mainly applicable to flexure-dominated restrained T-shaped RC beams within the investigated restraint coefficient κ range of 0.00–0.03. Its applicability to beams with different reinforcement ratios, restraint conditions, shear-span ratios, slab widths, and beam configurations requires further validation. Future studies will include additional tests with wider restraint levels and numerical parametric analyses to examine conditions that are difficult to realize experimentally, such as larger restraint stiffness levels and more refined restraint gradients. Digital image correlation measurements will also be incorporated to capture local deformation characteristics, including crack opening and bond-slip-related deformation. In addition, the current component-level findings will be extended to frame-level seismic design by evaluating the additional force demands imposed on columns and beam–column joints due to restraint-induced axial compression and beam overstrength.

Acknowledgments

This study is supported by the National Natural Science Foundation of China (52378515) and the Science and Technology Planning Project of Guangdong Province (2023A1111120027).

References

[1] M.S. Ashtiani, R.P. Dhakal, A.N. Scott, Seismic performance of high-strength self-compacting concrete in reinforced concrete beam-column joints, J. Struct. Eng. 140 (5) (2014) 04014002.

[2] R.C. Fenwick, A. Fong, The behaviour of reinforced concrete beams under cyclic loading, Bull. N. Z. Soc. Earthq. Eng. 12 (2) (1979) 158–167.

[3] T.S. Eom, H.G. Park, Elongation of reinforced concrete members subjected to cyclic loading, J. Struct. Eng. 136 (9) (2010) 1044–1054.

[4] R.V. Mehrabani, V. Sigrist, Elongation of reinforced concrete plastic hinges subjected to reversed cyclic loading, J. Struct. Eng. 141 (8) (2015) 04014188.

[5] M. Cooper, B.J. Davidson, J.M. Ingham, The influence of axial compression on the elongation of plastic hinges in reinforced concrete beams, in: Proc. New Zealand Concrete Industries Conf., 2005.

[6] H.E. Zerbe, A.J. Durrani, Seismic response of connections in two-bay R/C frame subassemblies, J. Struct. Eng. 115 (11) (1989) 2829–2844.

[7] R.C. Fenwick, L.M. Megget, Elongation and load deflection characteristics of reinforced concrete members containing plastic hinges, Bull. N. Z. Soc. Earthq. Eng. 26 (1) (1993) 28–41.

[8] E. Encina, Y. Lu, R.S. Henry, et al., Axial elongation in ductile reinforced concrete walls, Bull. N. Z. Soc. Earthq. Eng. 49 (4) (2016) 305–318.

[9] Z.N. Wu, D. You, X.L. Han, et al., Hysteresis elongation behavior of RC beams failing in different modes: Experimental investigation and numerical modelling using smeared crack approach, Eng. Struct. 329 (2025) 119807.

[10] J.Y. Lee, F. Watanabe, Predicting the longitudinal axial strain in the plastic hinge regions of reinforced concrete beams subjected to reversed cyclic loading, Eng. Struct. 25 (7) (2003) 927–939.

[11] J. Kim, J. Stanton, G. MacRae, Effect of beam growth on reinforced concrete frames, J. Struct. Eng. 130 (9) (2004) 1333–1342.

[12] S. Kokusho, S. Hayashi, A. Wada, et al., Behaviors of reinforced concrete beam subjected to the axial restriction of deformation, in: Proc. 9th World Conf. Earthq. Eng., Tokyo, Japan, 1988.

[13] E.I. Yang, S.T. Yi, S. Morita, Effect of axial restraint on flexural and shear behaviour of high-strength concrete members, Mag. Concr. Res. 56 (2) (2004) 63–72.

[14] S.T. Yi, E.I. Yang, Effect of axial restraint on mechanical behavior and average crack spacing of reinforced concrete flexural members, Nucl. Eng. Des. 228 (1–3) (2004) 107–117.

[15] J. Park, E. Strepelias, N. Stathas, et al., Application of hybrid simulation method for seismic performance evaluation of RC coupling beams subjected to realistic boundary condition, Earthq. Eng. Struct. Dyn. 50 (2) (2021) 375–393.

[16] K.K. Anaraki, J.W. Wallace, Analytical model for RC coupling beam considering axial restraint, Eng. Struct. 322 (2025) 119086.

[17] C.J. Motter, Reinforced concrete coupling beams with axial restraint, ACI Struct. J. 122 (1) (2025) 35–49.

[18] L. Wang, Y. Tian, W. Luo, et al., Seismic performance of axially restrained reinforced concrete frame beams, J. Struct. Eng. 145 (5) (2019) 04019019.

[19] W. Luo, L. Jiang, C. Lei, et al., Effects of axial restraints on beam flexural and joint shear behaviors in reinforced concrete frames under seismic loading, J. Earthq. Eng. 27 (1) (2023) 121–141.

[20] J.H. Kim, S.J. Han, H. Jeong, et al., Experimental evaluation of beam elongation phenomenon in precast concrete frame subjected to cyclic loading, J. Build. Eng. 110 (2025) 113094.

[21] X.L. Han, X.J. Chen, D.F. Huang, et al., Experimental study on seismic performance of RC beams considering axial constraints, Eng. Mech. (2024) (in Chinese).

[22] R.P. Dhakal, B.H. Peng, R.C. Fenwick, et al., Cyclic loading test of reinforced concrete frame with precast-prestressed flooring system, ACI Struct. J. 111 (4) (2014) 777–788.

[23] M. Masoudi, S. Khajevand, Revisiting flexural overstrength in RC beam-and-slab floor systems for seismic design and evaluation, Bull. Earthq. Eng. 18 (11) (2020) 5309–5341.

[24] B. Mihaylov, A. Trandafir, X. Palios, et al., Effect of axial restraint and loading history on the behavior of short reinforced concrete coupling beams, ACI Struct. J. 118 (4) (2021) 71–82.

[25] R.C. Fenwick, B.J. Davidson, Elongation in ductile seismic-resistant reinforced concrete frames, in: ACI Spec. Publ. 157, 1995, pp. 143–170.

[26] Z.N. Wu, A.Y. Elghazouli, X.L. Han, et al., Assessment and design of restrained reinforced concrete beams subjected to hysteresis elongation effects, Eng. Struct. 346 (2026) 121408.

[27] ACI Committee 318, Building Code Requirements for Structural Concrete (ACI 318-19) and Commentary (ACI 318R-19), American Concrete Institute, Farmington Hills, MI, 2019.

[28] CEN, EN 1998-1:2004 Eurocode 8: Design of Structures for Earthquake Resistance—Part 1: General Rules, Seismic Actions and Rules for Buildings, European Committee for Standardization, Brussels, 2004.

[29] Standards New Zealand, NZS 3101.1:2006 Concrete Structures Standard—The Design of Concrete Structures, Standards New Zealand, Wellington, 2006.

[30] Ministry of Housing and Urban-Rural Development of the People's Republic of China, GB 50011-2010 Code for Seismic Design of Buildings, China Architecture & Building Press, Beijing, 2016.

[31] M. Surana, Y. Singh, D.H. Lang, Effect of strong-column weak-beam design provision on the

seismic fragility of RC frame buildings, Int. J. Adv. Struct. Eng. 10 (2018) 131–141.
[32] Z.N. Wu, X.L. Han, A.Y. Elghazouli, et al., Assessment and design of RC frames incorporating effects of restraint to beam hysteresis elongation, J. Build. Eng. 120 (2026) 115600.
[33] H.E. Zerbe, A.J. Durrani, Seismic response of connections in two-bay reinforced concrete frame subassemblies with a floor slab, ACI Struct. J. 87 (4) (1990) 423–432.
[34] X.L. Han, Y.G. Qu, J. Ji, et al., A numerical study on the yielding mechanism of RC frame structure with cast-in-place slabs, Adv. Struct. Eng. 29 (3) (2026) 789–804.
[35] G. Santarsiero, A. Masi, Analysis of slab action on the seismic behavior of external RC beam-column joints, J. Build. Eng. 32 (2020) 101608.
[36] N. Ning, W.J. Qu, P. Zhu, Role of cast-in-situ slabs in RC frames under low-frequency cyclic load, Eng. Struct. 59 (2014) 28–38.
[37] Z. Zheng, X. Han, J. Ji, et al., Static mechanical properties of reinforced concrete beams considering structural spatial restraints: Experimental and numerical investigations, J. Build. Eng. 115 (2025) 114507.
[38] GB/T 50010–2010, Code for Design of Concrete Structures, Ministry of Housing and Urban-Rural Development of the People's Republic of China, Beijing, China, 2010.
[39] GB/T 50081–2019, Standard for test method of concrete physical and mechanical properties, Ministry of Housing and Urban-Rural Development of the People's Republic of China, Beijing, China, 2019.
[40] GB/T 228.1–2021, Metallic materials—Tensile testing—Part 1: Method of test at room temperature, Standardization Administration of China, Beijing, China, 2021.
[41] M. Tani, T. Mukai, T. Demizu, S. Kono, H. Kinugasa, M. Maeda, Full-scale static loading test on a five-story reinforced concrete building (Part 2: Damage analysis), in: Proceedings of the 16th World Conference on Earthquake Engineering, Santiago, Chile, 2017, Paper No. 1879.
[42] J. Ogawa, T. Shiga, Earthquake damage index for reinforced concrete columns, in: Proceedings of the 9th World Conference on Earthquake Engineering, Tokyo-Kyoto, Japan, 1988, Vol. IV, pp. 425–430.
[43] R. Park, Evaluation of ductility of structures and structural assemblages from laboratory testing, Bull. N. Z. Soc. Earthq. Eng. 22 (3) (1989) 155–166.
[44] B. Alfarah, J. Murcia-Delso, F. López-Almansa, S. Oller, RC structures cyclic behavior simulation with a model integrating plasticity, damage, and bond-slip, Earthq. Eng. Struct. Dyn. 47 (2) (2018) 460–478.
[45] W. Zhang, D.H. Lee, W.J. Lee, et al., Effect of cast-in-place beams on seismic performance of precast shear walls, ACI Struct. J. 120(1) (2022) 89–102.
[46] W. Zhang, S. Kim, D. Lee, et al., Comparative study on seismic performance of precast and reinforced concrete wide beam-column connections, Eng. Struct. 364 (2026) 123231.
[47] A. Hamoda, M. Ahmed, A. Abadel, et al., Synergistic strengthening of RC beams under torsion using NSM GSWR and steel bars: Experimental and numerical investigation, Structures 82 (2025) 110665.

Highlights

- Cyclic tests are conducted on T-shaped RC beams under axial restraint.
- Axial restraint suppresses axial elongation and alter its composition.
- A Restrained elongation induces axial compression and flexural overstrength.
- Slab action causes direction-dependent strength degradation and overstrength.
- FE analyses support compression–bending assessment of restrained T-shaped beams.

Declaration of interests

☒ The authors declare that they have no known competing financial interests or personal relationships that could have appeared to influence the work reported in this paper.

☐ The authors declare the following financial interests/personal relationships which may be considered as potential competing interests: